PAPER • OPEN ACCESS

Magnetooptical response of permalloy multilayer structures on different substrate in the IR–VIS–UV spectral range

View the article online for updates and enhancements.

Magnetooptical response of permalloy multilayer structures on different substrate in the IR–VIS–UV spectral range

Rajkumar Patra[1,9] , **Roland Mattheis**[2], **Hartmut Stöcker**[3],
Manuel Monecke[4], **Georgeta Salvan**[4] , **Rudolf Schäfer**[5,6],
Oliver G Schmidt[7,8] **and Heidemarie Schmidt**[1,2,9]

[1] Institute for Solid State Physics, Friedrich-Schiller University Jena, 07743 Jena, Germany
[2] Leibniz Institute of Photonic Technology IPHT, 07745 Jena, Germany
[3] Institute of Experimental Physics, TU Bergakademie Freiberg, 09596 Freiberg, Germany
[4] Semiconductor Physics, Chemnitz University of Technology, 09107 Chemnitz, Germany
[5] Leibniz Institute for Solid State and Materials Research (IFW), 01069 Dresden, Germany
[6] Institute for Materials Science, TU Dresden, 01062 Dresden, Germany
[7] Material Systems for Nanoelectronics, Chemnitz University of Technology, 09107 Chemnitz, Germany
[8] Institute for Integrative Nanosciences, IFW Dresden, 01069 Dresden, Germany

E-mail: rajkumar.patra@uni-jena.de and Heidemarie.Schmidt@leibniz-ipht.de

CrossMark

Abstract

The magnetooptical (MO) response of Ru/Py/Ta thin film stacks with 4, 8, and 17 nm thick $Ni_{81}Fe_{19}$ permalloy (Py) films on a SiO_2/Si and a ZnO substrate was measured by vector magnetooptical generalized ellipsometry. The MO response from VMOGE was modelled using a 4×4 Mueller matrix algorithm. The wavelength-dependent, substrate-independent and thickness-independent complex MO coupling constant ($\boldsymbol{Q}$) of Py in the Ru/Py/Ta thin film stacks was extracted by fitting Mueller matrix difference spectra in the spectral range from 300 nm to 1000 nm. Although the composition-dependent saturation magnetization of Ni_xFe_{1-x} alloys ($x = 0.0\dots1.0$), e.g. of $Ni_{81}Fe_{19}$, is predictable from the two saturation magnetization end points, the MO coupling constant of Ni_xFe_{1-x} is not predictable from the two $\boldsymbol{Q}$ end points. However, in a small alloy range ($0.0 < x < 0.2$ and $0.8 < x < 1.0$) the composition-dependent $\boldsymbol{Q}$ of Ni_xFe_{1-x} can be interpolated from a sufficiently high number of analyzed Ni_xFe_{1-x} alloys. The available complex MO coupling constants of six different Ni_xFe_{1-x} ($x = 1.0$ to 0.0) alloys were used to interpolate MO response of binary Ni_xFe_{1-x} alloys in the range from $x = 0.0$ to $x = 1.0$.

Keywords: magnetooptics, permalloy, magnetooptic coupling constant, Mueller matrix

(Some figures may appear in colour only in the online journal)

[9] Author to whom any correspondence should be addressed.

J. Phys. D: Appl. Phys. **52** (2019) 485002

R Patra *et al*

1. Introduction

In recent years, multilayers with magnetic materials have captivated ample interest in basic physics as well as in magnetic sensor and magnetic data storage applications because of their noticeable magnetooptical (MO) and magnetotransport properties [1–8]. Although the MO properties of nickel-iron based alloys, e.g. permalloy (Py) ($Ni_{81}Fe_{19}$), have been extensively studied experimentally with Kerr effect measurements [9, 10], a detailed analysis of Kerr angle and the deconvolution of the MO response of Py thin films in different multilayer stacks on different substrates are hardly reported in the literature. Although it has been vastly reported that surface roughness [11] and film thickness [12, 13] can modify the magnetic properties of Ni–Fe based material, the influence of film thickness and surface roughness on the MO response for this material is also scarcely found in literature. This suggests that an extensive study of the MO response for a similar multilayered stack of different thickness is needed to explore the modification of the MO properties with film thickness, surface roughness and underlying substrate of Ni–Fe based material.

Spectroscopic ellipsometry techniques have developed rapidly and were used to characterize reflected and transmitted polarized light at an oblique angle of incidence in the THz, infrared, visible, and UV spectral range from planar single and multilayer systems [14–20]. The inherent drawback of spectral ellipsometry is the data analysis in case of multilayer systems, which requires an optical model defined by the optical constants and layer thickness of each layer of the multilayer system [18]. According to the Onsager relation [21], below the Curie temperature (T_c), where a spontaneous magnetization ($\boldsymbol{M}$) appears, the off-diagonal elements of the dielectric tensor,

$$\varepsilon_{ij}(-\boldsymbol{M},\omega) = \varepsilon_{ji}(\boldsymbol{M},\omega) \tag{1}$$

are odd functions of magnetization $\boldsymbol{M}$, i.e. the magnetization induces optical anisotropy in a ferromagnet. Recently, spectroscopic ellipsometry has been applied extensively to study optically anisotropic materials including planar [22, 23] and sculptured [24] ferromagnetic layers. Since ellipsometry analysis of anisotropic multilayer systems becomes rather difficult, a data analysis procedure referred to as 4×4 matrix method [25] is generally employed to characterize the directly measured 4×4 Mueller matrix (*M*) which is defined as

$$M = \begin{pmatrix} M_{11} & M_{12} & M_{13} & M_{14} \\ M_{21} & M_{22} & M_{23} & M_{24} \\ M_{31} & M_{32} & M_{33} & M_{34} \\ M_{41} & M_{42} & M_{43} & M_{44} \end{pmatrix}. \tag{2}$$

It has to be noted that similar symbols (*M* and *M*) have been conventionally chosen for magnetization ($\boldsymbol{M}$) and the Mueller matrix (*M*), respectively. Mueller matrix ellipsometry has a well-recognized, significant advantage in case of depolarizing materials: Depolarization may arise due to scattering of light [26, 27], associated optics [28] and/or due to thermal effects. When samples have a depolarization effect and only the 2×2 Jones matrix (*J*) is measured instead of the 4×4 Mueller matrix (*M*), the totally polarized light used as a probe in

ellipsometry is transformed to partially polarized light so that a measurement error is introduced. For example, the Jones matrix in reflection is written as follows [18]

$$J = \begin{pmatrix} r_{pp} & r_{ps} \\ r_{sp} & r_{ss} \end{pmatrix}, \tag{3}$$

where r_{pp} and r_{ss} are the amplitude reflection coefficients for *p*-polarized reflected/*p*-polarized incident and *s*-polarized reflected/*s*-polarized incident light, respectively, and where r_{ps} and r_{sp} are the amplitude reflection coefficients for *p*-polarized reflected/*s*-polarized incident and *s*-polarized reflected/*p*-polarized incident light, respectively. The fundamental ellipsometric parameters such as the complex reflectance ratio (ρ_{sp}), the ratio of amplitude diminutions (ψ_{sp}) and the phase difference induced by the reflection (Δ_{sp}) are defined as

$$\rho_{sp} = \tan \Psi_{sp} \cdot e^{i\Delta_{sp}} = \frac{r_{sp}}{r_{ss}} \tag{4}$$

$$\Psi_{sp} = \arctan |\rho_{sp}| = \arctan \left| \frac{r_{sp}}{r_{ss}} \right| (0° \leqslant \psi_{sp} \leqslant 90°) \tag{5}$$

$$\Delta_{sp} = -\arg(\rho_{sp}) = -\arg \left(\frac{r_{sp}}{r_{ss}} \right) (0° \leqslant \Delta_{sp} \leqslant 360°). \tag{6}$$

If incident, *s*-polarized light is used as a probe, the complex Kerr angle (Φ_K) is given by the relation

$$\Phi_K = \Psi_{sp} + i\Delta_{sp} = \theta_K + i\eta_K \tag{7}$$

with Kerr rotation (θ_K) and Kerr ellipticity (η_K). As seen from equations (4)–(7), Φ_K is related to off-diagonal elements of the Jones matrix. Depolarization is an intrinsic error that is present in the Jones matrix. This error in the Jones matrix causes the Kerr angle and -ellipticity to be erroneous. Hence, the extraction of the MO coupling constant by fitting the Kerr angle and Kerr ellipticity comes out to be inaccurate. To avoid this, the Mueller matrix elements have been fitted to extract the MO coupling constants. Since the off-diagonal block of the Mueller matrix represents the anisotropy of the film, the differential off-diagonal elements (defined later in equation (13)) represent the anisotropy *change* in the sample due to application of magnetic field, i.e. the change in MO response of the film can be quantified by the differential Mueller matrix elements. This allows us to choose two differential off-diagonal elements, namely ΔM_{14} and ΔM_{23}, for fitting in order to extract the MO coupling constant.

The aim of the manuscript is the factorization of the off-diagonal MO dielectric tensor elements ε_{ij} into the MO coupling $\boldsymbol{Q}$ of electromagnetic waves to a magnetizable material and the magnetization $\boldsymbol{M}$ of the magnetizable material. We tested this factorization of ε_{ij} on six different multilayer-stack samples with a magnetizable layer, namely Py, measured and modelled MO effects in dependence on the material-specific, wavelength dependent MO coupling $\boldsymbol{Q}$ and on the material-specific and volume dependent magnetization $\boldsymbol{M}$. This work was motivated by a work from Buchmeier *et al* 10 years back [29]. Buchmeier *et al* did not factorize their modelled off-diagonal elements of the dielectric tensor K ($=\varepsilon_{ij}$) into

J. Phys. D: Appl. Phys. **52** (2019) 485002

R Patra *et al*

Table 1. Extracted results from fitting of the XRR data. Film thickness and interface roughness for different samples are extracted from XRR modeling keeping constant densities of Ru as $12.37\,g\,cm^{-3}$, of Py as $8.6\,g\,cm^{-3}$, of Ta as $16.65\,g\,cm^{-3}$, of Si as $2.33\,g\,cm^{-3}$, and of ZnO as $5.61\,g\,cm^{-3}$.

Sample	Thickness (nm)			Interface roughness (nm)			
	Ru	Py	Ta	Air/Ru	Ru/Py	Py/Ta	Ta/Subs
Py_4 Si	2.59 ± 0.09	4.09 ± 0.08	2.33 ± 0.05	0.27 ± 0.07	0.22 ± 0.02	0.13 ± 0.02	0.09 ± 0.02
Py_8 Si	2.44 ± 0.07	8.30 ± 0.11	2.47 ± 0.09	0.24 ± 0.07	0.07 ± 0.43	0.49 ± 0.11	0.39 ± 0.06
Py_{17} Si	2.50 ± 0.09	16.95 ± 0.03	2.31 ± 0.28	0.39 ± 0.05	0.31 ± 0.12	0.78 ± 0.20	0.70 ± 0.09
Py_4 ZnO	2.45 ± 0.08	4.14 ± 0.09	2.40 ± 0.05	0.32 ± 0.06	0.36 ± 0.13	0.30 ± 0.08	0.17 ± 0.11
Py_8 ZnO	2.51 ± 0.08	8.34 ± 0.12	2.38 ± 0.09	0.34 ± 0.05	0.25 ± 0.14	0.49 ± 0.10	0.34 ± 0.07
Py_{17} ZnO	2.45 ± 0.07	17.03 ± 0.18	2.38 ± 0.17	0.37 ± 0.05	0.18 ± 0.17	0.67 ± 0.15	0.56 ± 0.09

a wavelength dependent factor Q and into a magnetic field dependent factor M as we do. They reported the thickness dependent off-diagonal elements K of the dielectric tensor ε_{ij} of bcc Fe (0 0 1) films in a multilayer-stack sample [29]. To study the thickness effect on MO response, we have grown similar Ru/Py/Ta stacks of ultrathin Py films with a nominal thickness of 5, 10 and 20 nm fabricated in the same run on a SiO_2/Si substrate and on a ZnO substrate where Ta acts as buffer layer and Ru as protection layer. XRR data showed that correspondingly realized thickness of the Py films was systematically slightly smaller, namely 4, 8, and 17 nm. The optical constants for all layers in the multilayered stacks were determined from the dielectric polarization, which is strong in the 1000 nm thick dielectric SiO_2 and quite weak in the metals Ru, Py, and Ta as electric fields applied to metals lead to current flows. Above the Curie temperature ($T_c = 853$ K), the light propagation in Py is similar to that in isotropic materials. We have performed vector magneto-optical generalized ellipsometry (VMOGE) [30] measurements for applied magnetic field in all six directions ($\pm X, \pm Y, \pm Z$). The maximum MO effect is in polar geometry, i.e. for applied magnetic field along the $\pm Z$ direction. We have determined the MO dielectric tensor of Py by analyzing the 2×2 and 4×4 Muller matrix data of all multilayered Py samples in polar geometry up to an out-of-plane external magnetic field of 0.4 T [30]. It should be noted that, the Kerr rotation angle of typical Py layers is rather small (0.057 deg @403 nm [31]) in comparison to CrB_3 (3.47 deg @424 nm [32]) and to Bi-substituted YIG (1.36 deg @502 nm [33]). The knowledge of the MO dielectric tensor of magnetizable layers in multilayers sample will make it possible to model the complex Kerr angle data and Mueller matrix data of given multilayer samples. A maximized Kerr microscopy signal will help to analyze the dynamics of domain wall motion in the magnetizable layers of a multilayer samples, e.g. in Py layers which are widely used in magnetic memory stacks [34]. In this work we focus on the investigation of Py by VMOGE. It should be noted that Py is also strongly investigated by Kerr microscopy [30] and ferromagnetic resonance [35] measurements. The obtained MO coupling constant was validated by comparing literature data. Furthermore, the complex coupling constants of binary Ni_xFe_{1-x} alloys have been interpolated in the range $0 < x < 0.2$ and $0.8 < x < 1.0$. In the future, when VMOGE experiments and analysis has been extended to the THz, infrared, visible, and UV spectral ranges, the design

of planar multilayer stacks with a strong MO response by stacking an optimized sequence of magnetic, nonmagnetic metal, semiconductor, and dielectric layers and by using an optimized polarization state of incident and reflected light in the corresponding spectral range is envisioned.

2. Samples

A set of Ta (3 nm)/$Ni_{81}Fe_{19}$/Ru (3 nm) planar stacks with 4 nm, 8 nm, and 17 nm nominal thickness of the $Ni_{81}Fe_{19}$ (Py) layers has been prepared by means of DC magnetron sputtering and using an industrial UHV system (base pressure below 2×10^{-8} mbar). The system is equipped with sputtering targets of 300 mm diameter. The thickness homogeneity, verified by optical methods was better than 2% over a diameter of 200 mm. Sputtering of Ta, Py and Ru was carried out at a pressure of 5×10^{-3} mbar in 6N Ar. During sputtering of the Py layer an in-plane magnetic field of 5 mT was applied to induce a well-defined deposition induced anisotropy axis with an anisotropy field H_k of 0.5 mT (~0.4 kA m^{-1}) [36–38].

In order to explore the underlying substrate effect on MO coupling constant, the same planar stack has been deposited on two different substrates, thermally oxidized Si and ZnO. The deposition was performed on a 6″ thermally oxidized Si/SiO_2 (1000 nm) wafer with a $1 \times 1\,cm^2$ square ZnO substrate located in the center of the 6″ Si/SiO_2 substrates.

The 3 nm thick Ta buffer layer serves as a seed layer to induce a growth of the Py with a pronounced ⟨1 1 1⟩ texture and guaranties a well-defined magnetic softness. The 3 nm thick Ru layer on top of the stack serves as a protection layer to prevent oxidation of the underlying Py layer.

3. Experiments

3.1. Structural and magnetic properties of the Py layer on Si/SiO_2 and ZnO

The use of x-ray diffraction (XRD) confirmed the expected ⟨1 1 1⟩ texture. X-ray reflectivity (XRR) was used to determine the thickness of the individual layers and the interfacial roughness within the stack. For the simulation of the XRR data (see figure 1 and table 1), fixed densities of the different layer materials (see caption in table 1) within the multilayer
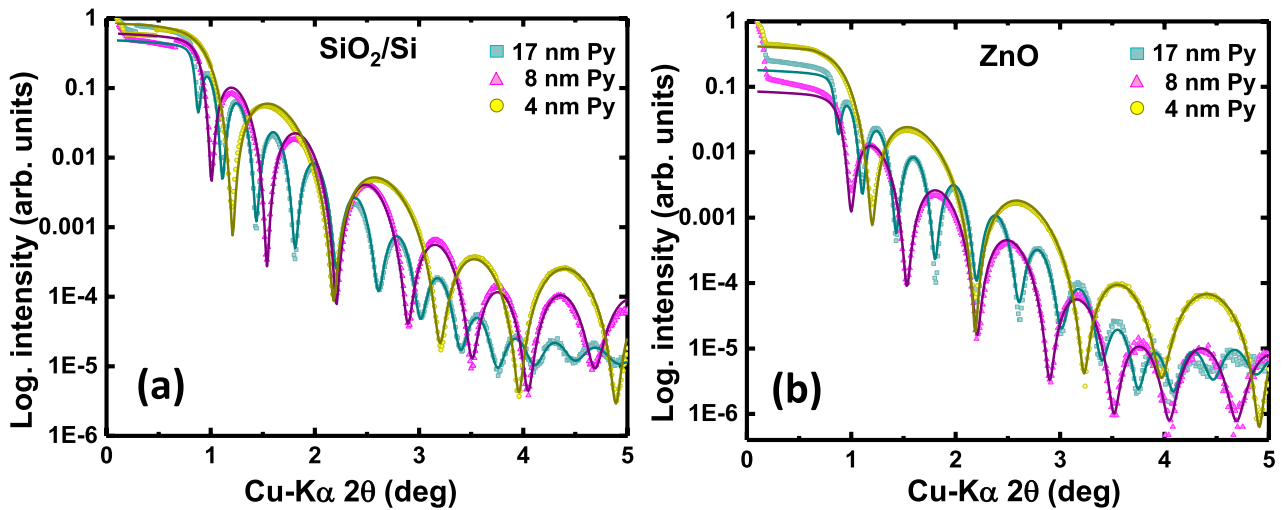
J. Phys. D: Appl. Phys. **52** (2019) 485002

R Patra *et al*

Figure 1. XRR patterns of 17 nm (cyan symbols), 8 nm (magenta symbols), 4 nm (yellow symbols) thin Py films with a 3 nm thick Ru protection layer and a 3 nm thick Ta adhesion layer (a) on a 1000 nm SiO$_2$/Si substrate and (b) on a ZnO substrate. The solid lines in respective color show the fitting of corresponding data.
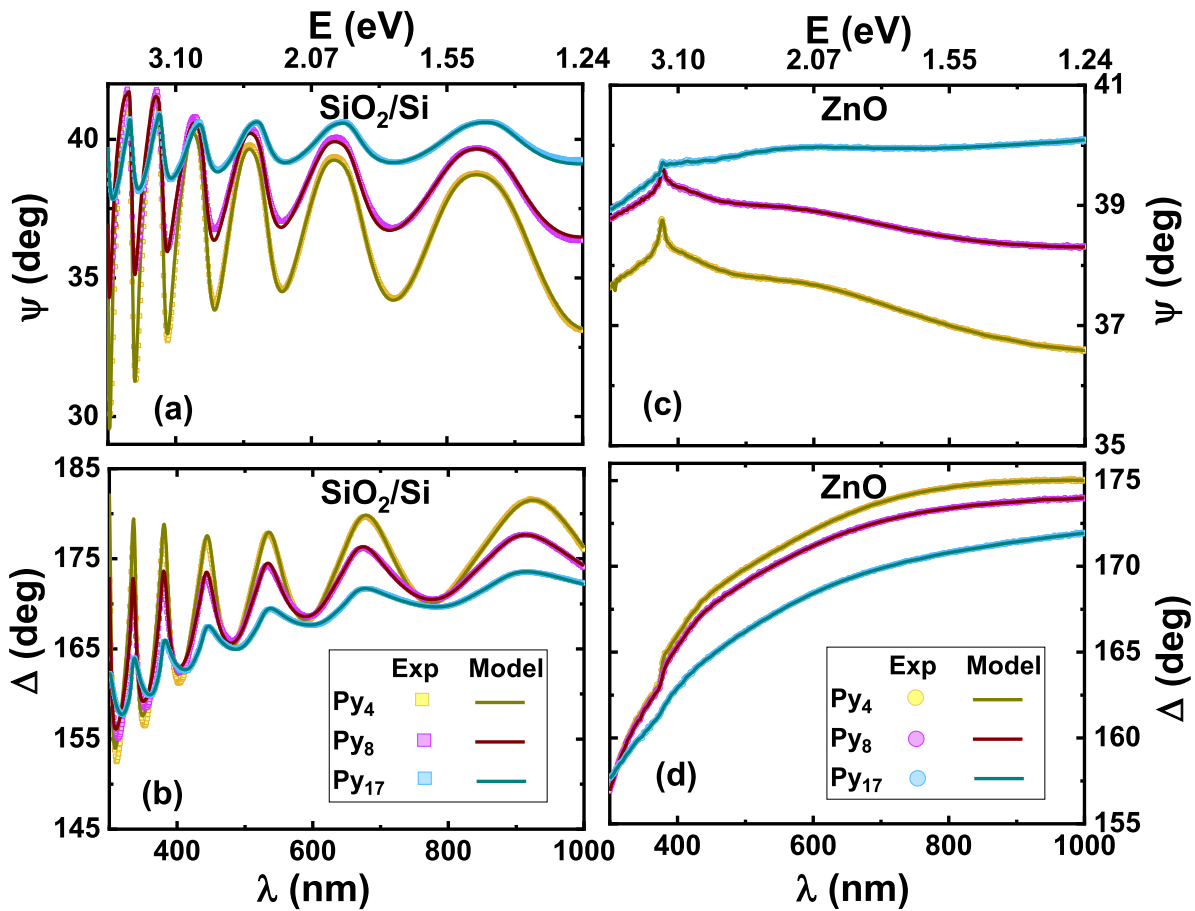

Figure 2. Experimental and fitted ψ and Δ plot for 4 nm, 8 nm and 17 nm Py samples on (a) and (b) SiO$_2$/Si and ((c) and (d)) on ZnO. The perfect fitting of the experimental data discards the presence of any scattering effect at the SiO$_2$/Si interface.

stack were used. Since the thickness of the SiO$_2$ layer amounts to 1000 nm, the SiO$_2$/Si interface cannot be resolved from XRR data.

As seen from the XRR results (table 1), all values are identical for both substrates within the measurement error. Due to thickness roughness of the thicker Py films, the simulated value for the Py/Ta and Ta/Substrate interface roughness increases with increasing Py thickness starting at 0.10 ± 0.04 nm for Si/SiO$_2$ and 0.25 ± 0.10 nm and increases to 0.8 ± 0.2 nm (Si/SiO$_2$) and 0.6 ± 0.15 nm for ZnO.

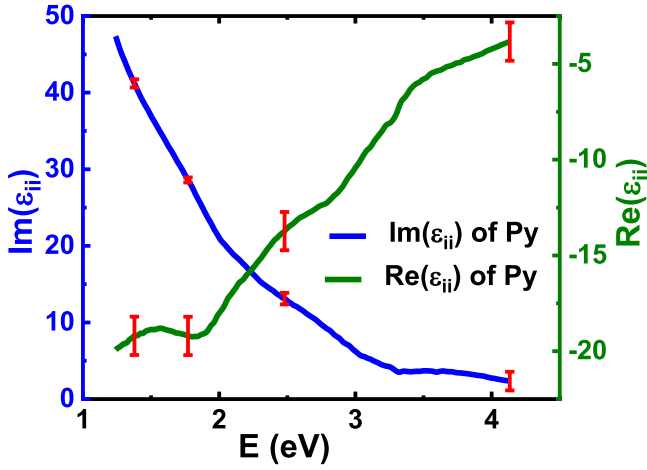Kerr loop tracer magnetometry (not shown) was used to verify the softness of the films. A well-established easy axis

J. Phys. D: Appl. Phys. **52** (2019) 485002

R Patra *et al*

Figure 3. Modeled complex on-diagonal elements of the MO dielectric tensor ε_{ii} of Py which is the same for all six samples. The material-specific on-diagonal elements ε_{ii} are independent of the Py thickness and underlying substrate. To be noted, Re(ε_{ii}) is dispersive and Im(ε_{ii}) is absorptive. Layer thicknesses extracted from XRR (table 1) have been used as fixed parameters. Errors (red error bars) in the on-diagonal dielectric tensor ($\delta(\varepsilon_{ii})$) are given at 300 nm, 500 nm, 700 nm, and 900 nm.

($H_C < 0.02$ mT), and hard axis ($H_k = 0.5$ mT) was found as usual for soft NiFe films. By using SQUID magnetometry, the magnetization was determined to 105 ± 15 emu g^{-1} for Py$_{17}$Si and Py$_{17}$ ZnO. Saturation magnetization for perpendicular orientation was obtained at $\mu_0 H = 1.3$ T.

3.2. Spectral ellipsometry

The layer thickness and surface roughness, extracted from the XRR measurements, are used as fixed parameters for modelling the spectroscopic ellipsometry data (for detailed discussions, see section 3.3) for all samples (using CompleteEASE software), to find out the optical constant and hence dielectric constant of each layer (figure 2) in all samples. We have used a combination of one Drude (describing free electrons) and three Tauc–Lorentz (describing interband transitions) oscillators to parameterize the optical constant of the Py layer for each sample. The presence of any scattering effect at the SiO$_2$/Si interface is discarded by a perfect fitting of the experimental data for all samples on the SiO$_2$/Si substrate (figures 2(a) and (b)). Observed oscillations in spectroscopic ellipsometry plot as well as MO plots of samples on SiO$_2$/Si are thickness fringes which arise due to the 1000 nm thick SiO$_2$ layer. A sharp peak, representing the optical transition of ZnO, is visible at 3.3 eV [39] in the ψ plot on the ZnO substrate (figure 2(c)).

Figures 3 and 4 shows that the obtained on-diagonal elements of the complex dielectric constant and complex MO conductivity of the Py layer is material-specific and thickness-independent. The plasma frequency calculated from the Drude oscillator parameter is found to be 12.00 eV which is almost similar to the reported value by Tikuišis *et al* [40]. Furthermore, the value is consistent with the constituents Ni (7–15.92 eV) [41–43] and Fe (10–12 eV) [42]. On-diagonal permittivity spectra (figure 3) show a typical metallic behavior which is analogous to that of pure Ni, Fe and other closely

related metal films like Cu [40–44]. The strong peak around 1.5 eV of the Re(ε_{ii}) spectra can be compared to the 1.4 eV shoulder of the Ni spectra which arises due to a transition between the W and K points in the Brillouin Zone. In another report, Smith *et al* reported that this peak arises in pure Ni due to spin–orbit spitting. This peak may be attributed to two transitions in k-space vicinity namely, a temperature dependent b-transition (minority spin band to final states above E_F) and a temperature independent b'-transition (between bands $5 \rightarrow 6$ for both spins) [45]. The shift (from 1.4 eV toward 1.5 eV) in this peak can be attributed to the presence of Fe in Py. The weak peak at 2.3 eV is referred as a temperature-dependent c-transition between the bands $2 \rightarrow 5$ (minority spin band to final states above E_F). The peak around 2.5 eV in the same spectra can be identified as arising from transition X_4 [44]. This peak can also be found in Fe spectra, corresponding to a transition in the zone face (direction K and points P) [40, 42]. The optical response of a material within magnetic field can be described equivalently by the on-diagonal elements of the MO conductivity tensor, which are related to the on-diagonal elements of the MO dielectric tensor as follows [46]:

$$\sigma_{ii} = \frac{i\omega(1 - \varepsilon_{ii})}{4\pi}. \tag{8}$$

Using equation (8), the modeled dispersive (real) and absorptive (imaginary) parts of the on-diagonal elements of the dielectric tensor (see figure 3) were further used to calculate the dispersive (imaginary) and absorptive (real) parts of the on-diagonal elements of the MO conductivity tensor (figures 4(a) and (b)). Later, we will introduce the off-diagonal elements of the magneto-optical conductivity tensor to describe the optical response of a material with magnetic field, named 'magneto-optical response'.

3.3. Vector magneto-optical generalized ellipsometry (VMOGE)

The 4 × 4 Mueller matrix has been measured in a 3D magnetic field setup by a vector magneto-optical generalized ellipsometer (VMOGE) which combines a rotating compensator ellipsometer RC2 from J.A. Woollam Co., Inc., USA. with a custom-built 0.4 T octupole magnet sample stage. VMOGE allows to access both the 2 × 2 Jones matrix (equation (3)) and the complete 4 × 4 Mueller matrix (equation (2)) in a magnetic field up to 0.4 T of arbitrary direction and in the spectral range from 300 to 1000 nm (with spectral resolution of 1 nm). The VMOGE experimental coordinate system is defined as follows: the x- and y-axis are aligned parallel and perpendicular to the plane of incidence, respectively, and both axes lie in the sample surface plane. The z-axis is normal to the sample surface and points into the sample. Three VMOGE configurations, longitudinal (L), transverse (T), and polar (P) are conventionally defined according to the direction of applied magnetic field vector $\boldsymbol{H} = (H_x, H_y, H_z)$ with respect to the plane of incidence and the sample surface plane. For $\boldsymbol{H}$ within the Cartesian coordinate system of the VMOGE setup, the MO properties of the ultrathin Py layer are described by the following MO dielectric tensor ε^{MO}:
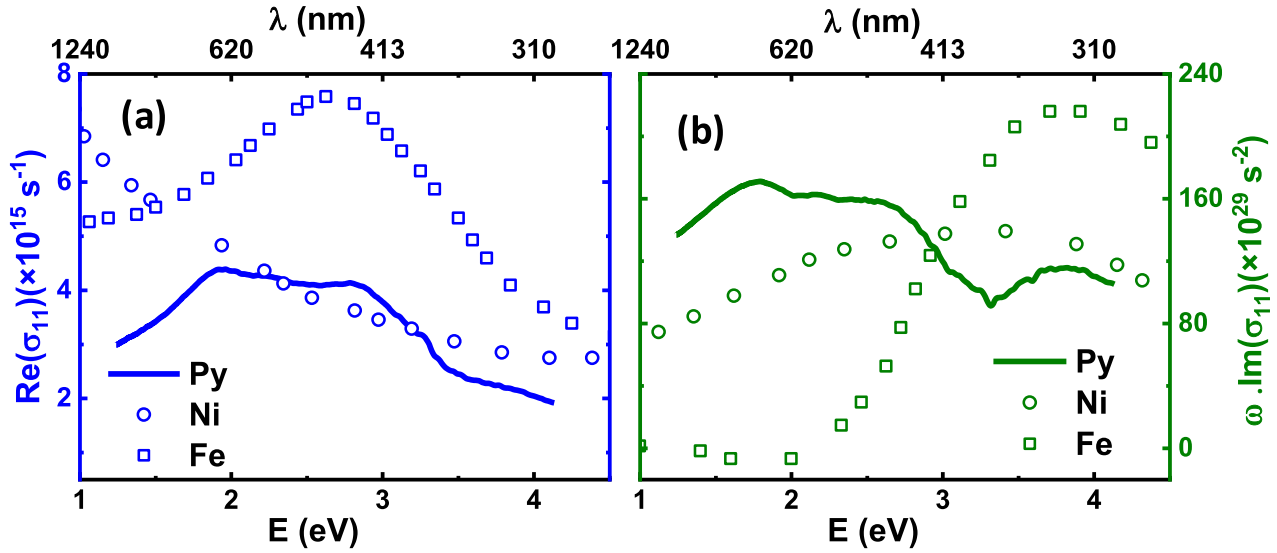
J. Phys. D: Appl. Phys. **52** (2019) 485002

R Patra *et al*

Figure 4. Calculated (a) real and imaginary (b) on-diagonal elements of the MO conductivity tensor σ_{11} of Py which is the same for all six samples. The material-specific on-diagonal elements of conductivity tensor σ_{11} are independent of the Py thickness and underlying substrate. (a) and (b) Circles in respective color show the corresponding plot for fcc Ni and squares in respective color show the corresponding plot for bcc Fe [47]. In contrast to figure 3, here $\text{Im}(\sigma_{ii})$ is dispersive and $\text{Re}(\sigma_{ii})$ is absorptive.

$$\varepsilon^{MO} = \begin{bmatrix} \varepsilon_{xx} & \varepsilon_{xy} & \varepsilon_{xz} \\ \varepsilon_{yx} & \varepsilon_{yy} & \varepsilon_{yz} \\ \varepsilon_{zx} & \varepsilon_{zy} & \varepsilon_{zz} \end{bmatrix} = \begin{bmatrix} \varepsilon_{xx} & -iQ_zM_z & -iQ_yM_y \\ iQ_zM_z & \varepsilon_{yy} & -iQ_xM_x \\ iQ_yM_y & iQ_xM_x & \varepsilon_{zz} \end{bmatrix},$$

(9)

where the on-diagonal terms ε_{ii}, $ii = xx$, yy, zz of MO dielectric tensor of Py are equal, representing the square of the complex refractive index. The off-diagonal, nonsymmetric terms ε_{ij}, $(i, j = x, y, z)$ are assumed to depend on the magnetization vector $\boldsymbol{M} = (M_x, M_y, M_z)$ and on the complex MO coupling constant $\boldsymbol{Q} = (Q_x, Q_y, Q_z)$ [22, 23]. It is important to clarify that there exist different sign conventions to describe the MO dielectric tensor. According to optics convention of optical constants [18], the MO coupling constant is defined as $\boldsymbol{Q} = \text{Re}(\boldsymbol{Q}) - i\text{Im}(\boldsymbol{Q})$. If the magnetization $\boldsymbol{M}$ of the investigated samples is parallel to the magnetic field $\boldsymbol{H}$ (i.e. $\boldsymbol{M} \parallel \boldsymbol{H}$), for P-VMOGE with $\boldsymbol{H} = (0, 0, H_z)$, it holds that $\boldsymbol{M} = (0, 0, M)$. Please note that the MO coupling constant is different from the Voigt constant also commonly denoted with Q but defined as $\varepsilon_{xy} = iQ\varepsilon_{xx}$ [48].

The MO response can be described equivalently by the off-diagonal elements of the MO conductivity tensor, which are related to the off-diagonal elements of the MO dielectric tensor as follows [22, 46]

$$\sigma_{ij} = -\frac{i\omega\varepsilon_{ij}}{4\pi}.$$

(10)

σ_{ij} is calculated from the spin-polarized bandstructure and used to investigate the microscopic origin of the MO effects as a combined action of spin–orbit coupling and net spin-polarization [41]. In order to remove offset effects in the large field range, we have modeled MO difference spectra, which are defined for the components of complex Kerr angle as follows:

$$\Delta\theta_K = \theta_K(-H_z) - \theta_K(+H_z)$$

(11)

$$\Delta\eta_K = \eta_K(-H_z) - \eta_K(+H_z).$$

(12)

We measured the MO response of similar Ru/Py/Ta stacks on a SiO_2/Si substrate and a ZnO substrate using 2×2 Jones matrix and 4×4 Mueller matrix ellipsometry in a 0.4 T octupole magnet [30] at 300–1000 nm wavelength range. To obtain optimized MO and optical response, we have chosen 45° as angle of incidence of polarized light during the VMOGE measurements. The experimental data was modeled using the optical constants of each layer of the multilayer system as obtained from fitting of the spectroscopic ellipsometric data.

Figures 8 and 9 show all Mueller matrix elements for the Py_{17} samples (thickest in the series) on SiO_2/Si and ZnO substrate, respectively. The difference in MO response is seen to be maximum for four Mueller matrix elements, namely M_{14}, M_{41}, M_{23} and M_{32}, when a magnetic field of 0.4 T is applied along the $\pm z$ direction for the Py samples on both substrates. Physically, M_{14} $(-M_{41})$ represents circular dichroism (CD) and M_{23} $(-M_{32})$ represents circular birefringence (CB) of a depolarizing sample [49]. These results also confirm the presence of both, exchange splitting and spin–orbit interaction for Py in the external magnetic field [45]. Distinct differentiable Magneto-optic responses (M_{14}, M_{41}, M_{23} and M_{32}) are found in the lower energy region below 3.0 eV, which is typical for Drude behavior. The most significant MO active electron transitions occur between the 3d and unpolarized 4s band. [40]

A better match between experimental and modeled MO data in the spectral range from 300 nm to 1000 nm can only be found if the 4×4 Mueller matrix is measured and modeled. As we have concluded from the previous plots (figures 5 and 6), the following Mueller matrix elements M_{ij} are strongly dependent on the magnetization of the Py thin films: M_{14}, M_{23}, M_{32}, M_{41}. Using the analogue of Kerr angle difference spectra (equations (11) and (12)), we define the Mueller matrix element difference spectrum (ΔM_{ij}) of a given Mueller matrix element M_{ij} as follows:

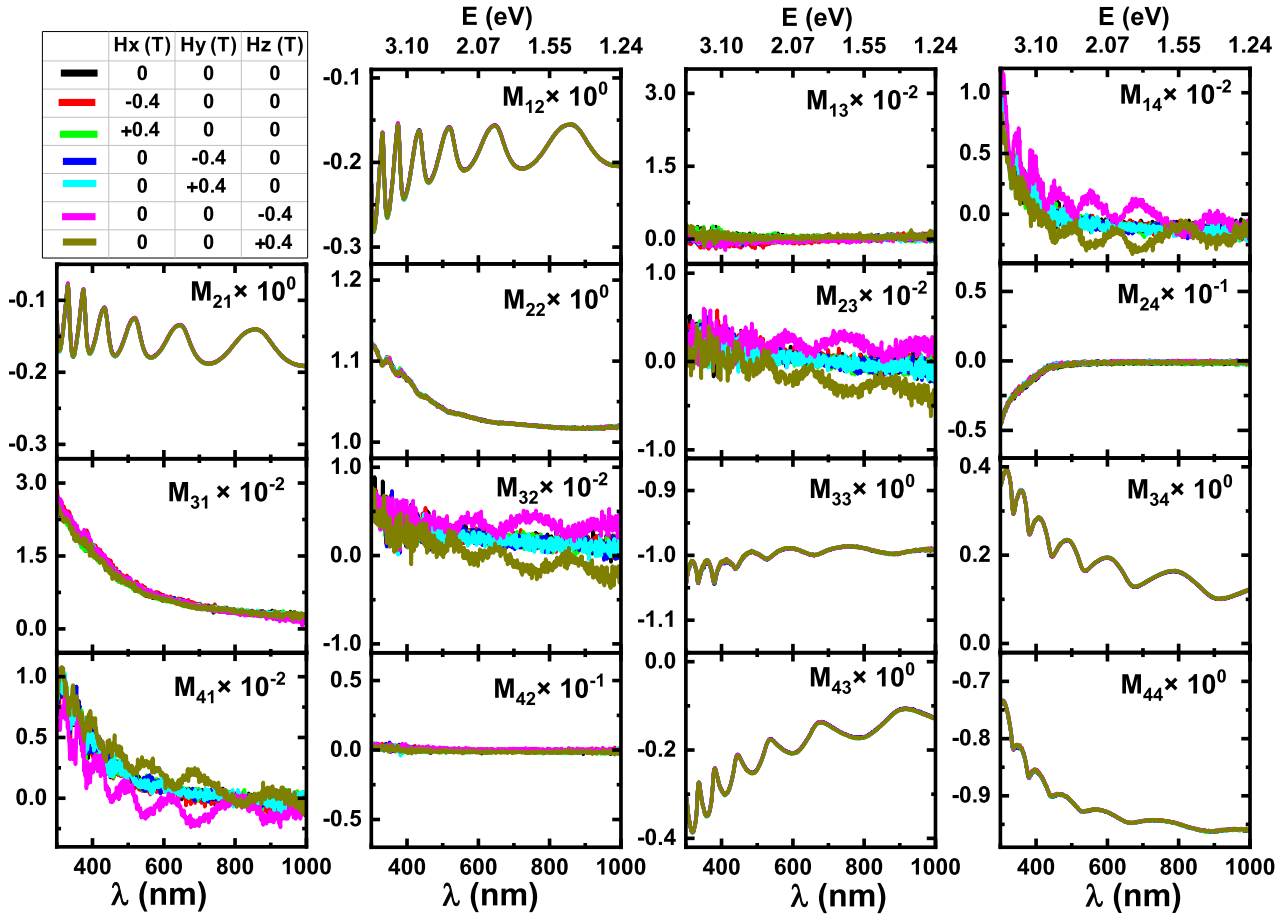$$\Delta M_{ij} = M_{ij}(-H_z) - M_{ij}(+H_z).$$

(13)

Figure 5. All Mueller matrix element plot of Py_{17} on SiO_2/Si substrate for applied magnetic field in all six directions ($\pm X$, $\pm Y$, $\pm Z$) and at zero magnetic field condition (see top-left corner table in this plot). From this plot one can conclude that M_{14}, M_{41}, M_{23} and M_{32} shows the maximum MO effect along the $\pm z$ magnetic field direction, which constrain us to consider these four elements for further calculations of the MO coupling constant.

Using the extracted off-diagonal elements of the dielectric tensor of Py in the multilayer structures, we performed a point-by-point fit with the Mueller matrix element difference data ΔM_{14} and ΔM_{23} (figure 7) by the 4×4 transfer matrix method (since $|\Delta M_{41}|$ and $|\Delta M_{32}|$ are similar to $|\Delta M_{14}|$ and $|\Delta M_{23}|$, respectively).

Figure 8 shows the measured and modelled complex Kerr angle difference spectra of 4 nm, 8 nm and 17 nm thick Py layers in the Ru/Py/Ta stack on SiO_2/Si substrate (figures 8(a)–(c)) and on the ZnO substrate (figures 8(d)–(f)). The complex Kerr angle data have been modeled using the 2×2 Jones matrix approach and the extracted thickness-independent and wavelength-dependent dielectric tensor (figure 2). Due to the intrinsic measurement error (discussed in section 1) of the 2×2 Jones matrix in case of depolarization and anisotropy effects, no unique solution for the extracted off-diagonal dielectric tensor elements of Py (figure 9(b)) can be found. That causes the mismatch between measured and modeled Kerr angle in the spectral range between 300 nm and 400 nm (figure 8). Thickness fringes are fitted well with the ellipsometric angles ψ and Δ (figure 2). From that, we can conclude that there is no density gradient in the SiO_2 layer and there is no scattering present at the SiO_2/Si interface which would degrade the thickness fringes.

4. Discussion of MO response

The off-diagonal dielectric tensor is plotted with error bars in figure 9(a). In contrast to the on-diagonal dielectric part, for the off-diagonal dielectric tensor $Re(\varepsilon_{12})$ is absorptive and $Im(\varepsilon_{12})$ is dispersive. From the fitting of the difference spectra, the wavelength-dependent MO coupling constant (Q) of the Py layer in the multilayer stack on SiO_2/Si substrate and on ZnO substrate has been calculated. Similar Q values have been found for all samples within the error range (figure 9(b)). The zero crossing position, which relates physically to the width of the d-band [50, 51], has been found at 2.03 eV for both, imaginary part of the off-diagonal dielectric constant and the real part of the MO coupling constant. We have also compared the obtained result with reported values and found excellent agreement [22, 52]. The obtained $Q(\lambda)$ has been validated for different thicknesses of Py in the same multilayer stack on both, SiO_2/Si and ZnO substrate to confirm the thickness independency of the MO coupling constant. As expected and demonstrated in figure 8 the modelled MO coupling constant of Py depends on the wavelength but not on the structure of the multilayer sample and also not on the thickness of Py layer. The goodness of fit, defined by MSE [53], amounts to 0.817 considering the total weightage of ΔM_{14} and
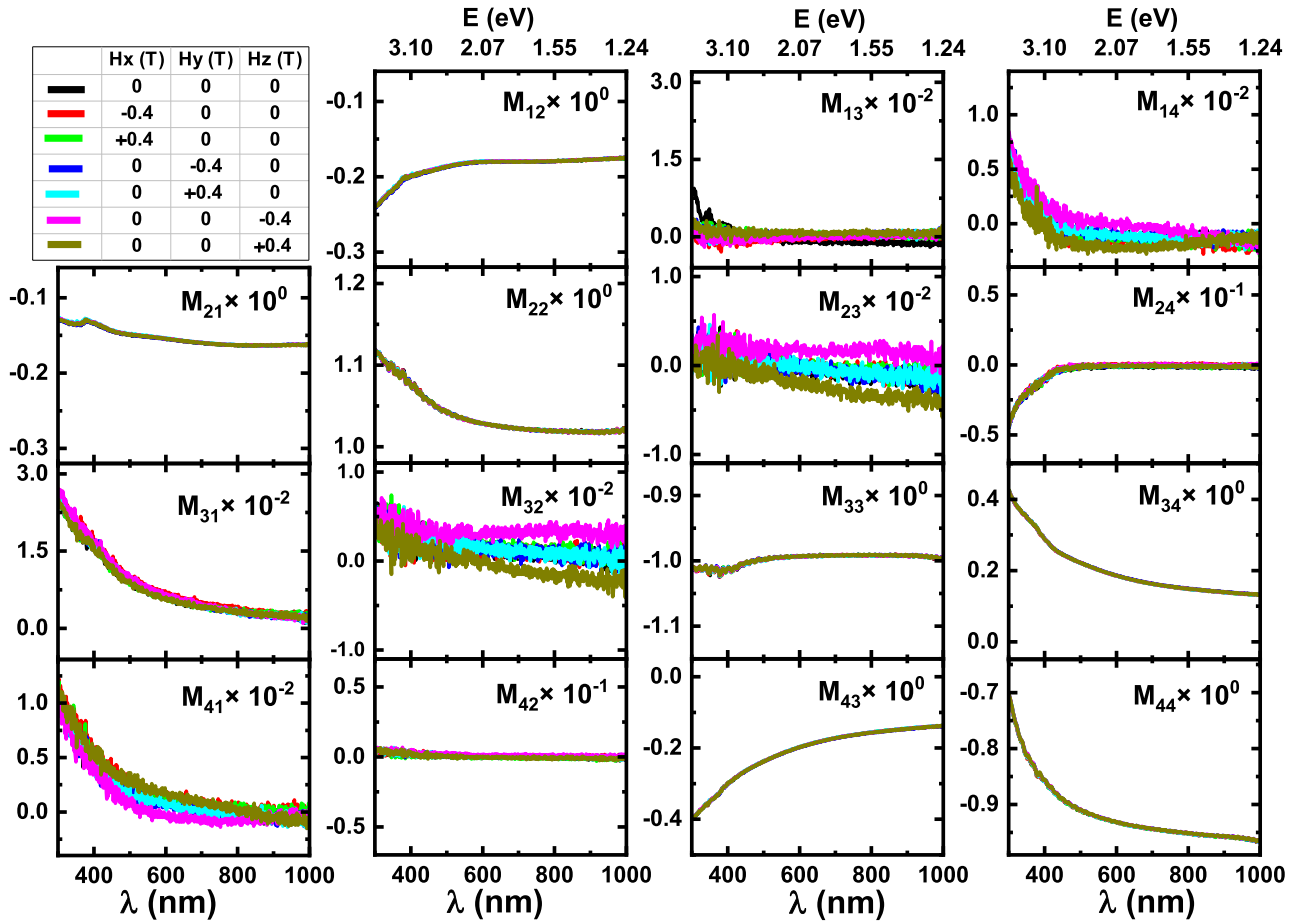
J. Phys. D: Appl. Phys. **52** (2019) 485002

R Patra *et al*

Figure 6. All Mueller matrix element plot of Py_{17} on ZnO substrate for applied magnetic field in all six directions ($\pm X$, $\pm Y$, $\pm Z$) and no magnetic field condition (see top-left corner table in this plot). From this plot one can conclude that M_{14}, M_{41}, M_{23} and M_{32} shows the maximum MO effect along $\pm z$ magnetic field direction which compel us to consider these four elements for further calculation of MO coupling constant.

ΔM_{23}. There is no surface roughness dependence found on $Q(\lambda)$. From this result we can conclude that the MO coupling constant $Q(\lambda)$ of a given material in a planar stack is independent of thickness [20], surface roughness and underlying substrate. Furthermore, we can comment that $Q(\lambda)$ does not depend on interface roughness and it is a bulk parameter. By compiling our result with other reported data [19, 52, 54, 55], the variation of saturation magnetization with Ni concentration in Ni_xFe_{1-x} alloys is plotted in figure 10(c). Our result falls onto a linear interpolation curve of the literature data, from which one can conclude that the saturation magnetization can be linearly interpolated for any composition of a binary Ni–Fe alloy. Figures 10(d) and (e) shows the variation of $Re(Q)$ and $Im(Q)$ with Ni concentration in Ni_xFe_{1-x} alloys at three different wavelengths (400 nm, 600 nm and 800 nm). From these plots one can see that the variation of $Re(Q)$ increases with an increment of Ni concentration for higher wavelength (800 nm). Same variation in $Im(Q)$ is visible at higher wavelength (800 nm). This suggests a good increment of the MO response at higher wavelengths, leading to the conclusion that at higher wavelength highly concentrated Ni-rich Ni_xFe_{1-x} material will be a better suited for MO sensor as compared to their low concentration counterpart. This results also implies that the complex MO coupling constant Q can be

interpolated when a sufficiently large number of Ni-Fe binary sample data is available.

The error bars in the extracted MO coupling constant ($\delta(Q)$) are given at 300 nm, 500 nm, 700 nm and 900 nm. The error ($\delta(Q)$) has been determined by neglecting the error in the magnetization measurements, as follows: $\delta(Q) = \delta(\varepsilon)/M$. The error of the dielectric tensor ($\delta(\varepsilon)$) has been determined by modelling the off-diagonal elements of the dielectric tensor at maximum possible Mueller matrix difference ($\varepsilon_{max} = \varepsilon_{max}(\overline{\Delta MM} + (\delta(\Delta MM)))$) and the minimum possible Mueller matrix difference ($\varepsilon_{min} = \varepsilon_{min}(\overline{\Delta MM} - (\delta(\Delta MM)))$), not by the mean value of the Mueller matrix element and calculated data (see also error bars in figure 7). The error of the off-diagonal elements of the dielectric tensor is given by $\delta(\varepsilon) = |\varepsilon_{max} - \varepsilon_{min}|$.

Figures 11(a) and (b) shows the calculated real and imaginary part of the off-diagonal elements of the MO conductivity tensor plotted as a function of wavelength for Py material, which has been extracted from the difference spectra at an applied magnetic field of 0.4 T. Each plot is compared with the respective contribution of fcc Ni and bcc Fe [47]. According to Delin *et al* [47], breaking of time-reversal symmetry in the lattice structure of Py, under the application of external magnetic field during a MO measurement with the magnetic field
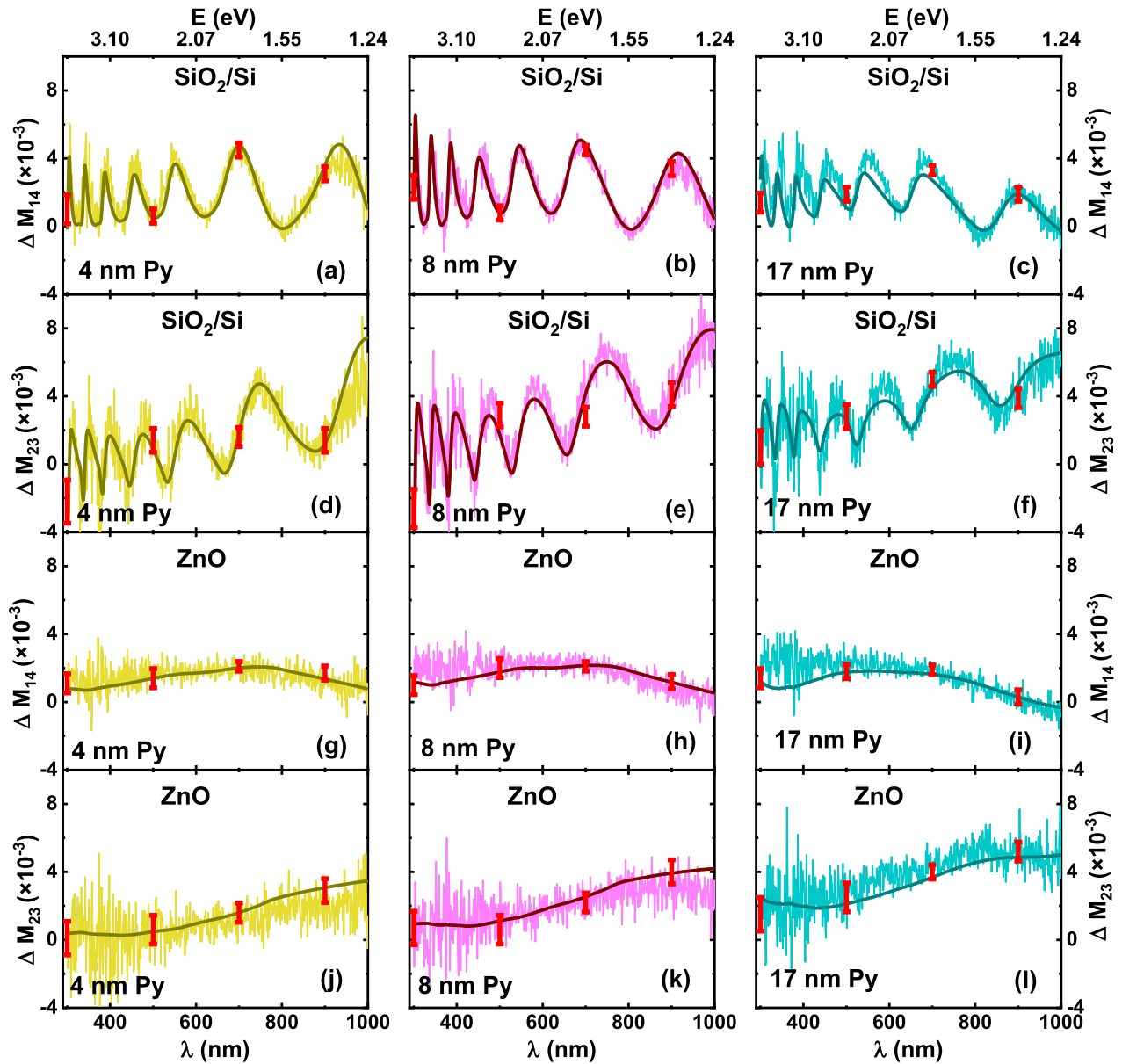
Figure 7. Experimental (faded thin line) and modeled (dark thick line) Mueller matrix element difference spectra (equations (13)) (a)–(c) ΔM_{14} and (d)–(f) ΔM_{23} on SiO_2/Si substrate and (g)–(i) ΔM_{14} and (j)–(l) ΔM_{23} of the 4 nm, 8 nm, 17 nm thick Py layer in the Ru/Py/Ta stack on ZnO substrate. The Mueller matrix difference spectrum has been recorded as a function of wavelength at 45° angle of incidence and a magnetic field of 0.4 T in the 4 × 4 matrix algorithm. Errors (red error bars) in the Mueller matrix difference data ($\delta(\Delta MM)$) are given at 300 nm, 500 nm, 700 nm and 900 nm.

applied perpendicular (*z*-direction) to the plane of light polarization (*x-y* plane), causes magneto-optic effects due to which the system reacts differently to photons with helicity −1 (spin is antiparallel to momentum) in comparison to photons with helicity +1 (spin is parallel to momentum). Furthermore, those authors have stated that the real part of the on-diagonal MO conductivity tensor (figure 3) is physically related to ordinary optical absorption, whereas the imaginary part of the off-diagonal MO conductivity tensor (figure 10) is physically related to MO absorption. The amount of MO absorption is directly proportional to the difference in absorption of left and right circularly spin polarized light. Its sign is associated with the spin polarization of the states responsible for interband transitions. The zero crossing position is found at 2.03 eV (same as

in figure 9), shifted from 5.0 eV for pure Ni [40]. This implies a shift of the *d*-band to higher energies. The energy shifts in the *d*-band vigorously rely on the lattice spacing and atomic coordination number. Permalloy lattice spacing (~3.546 Å) [58], which is 1% higher than that of pure Ni, 24% higher than that of pure Fe [40], 7% higher than that of Ta and 31% higher than that of Ru, may cause lattice mismatches at the Py/Ta and Ru/Py interfaces and may lead to red-shift in zero crossing position. A thickness dependency of the zero crossing position is not observed for our samples. The maximum MO off-diagonal conductivity below 3.0 eV energy confirms a typical Drude behavior [40] that we have already found earlier by the presence of a Drude oscillator in our fitting model. The dispersion of the MO conductivity of Py is mainly due to the strong
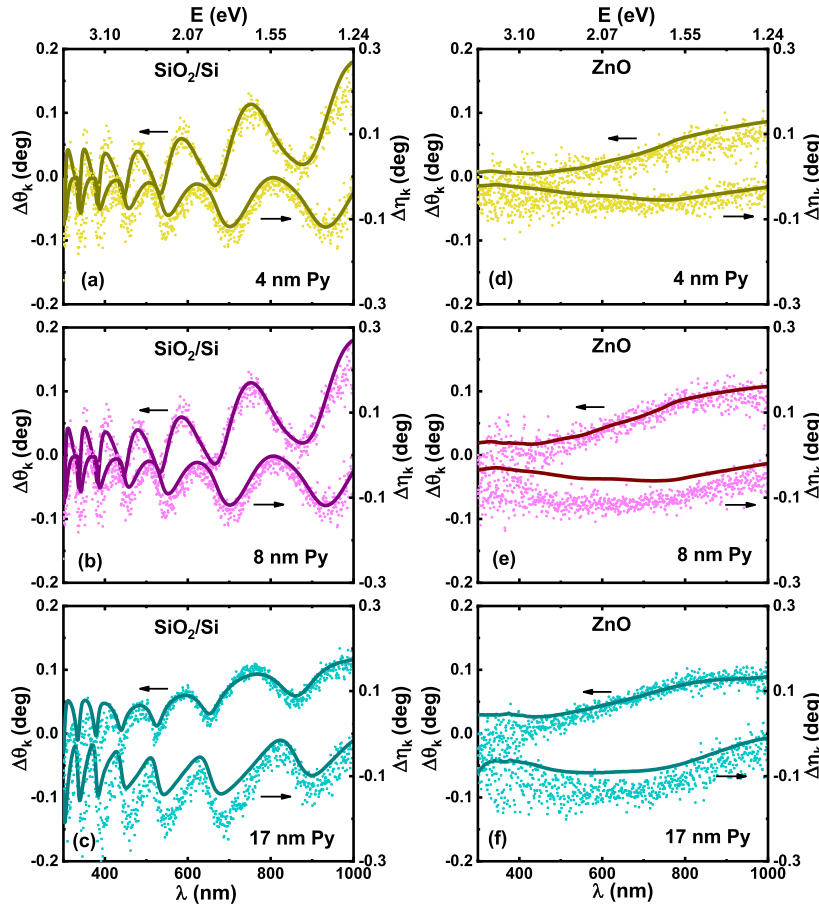
Figure 8. Experimental (solid line) and modeled (scattered dots) complex polar Kerr angle difference spectra (equations (11) and (12)) of the 4 nm, 8 nm, 17 nm thick Py layers in the Ru/Py/Ta stack (a)–(c) on SiO$_2$/Si substrate and (d)–(f) on ZnO substrate. The Kerr rotation difference spectrum ($\Delta\theta_K$) and the Kerr ellipticity difference spectrum ($\Delta\eta_K$) are recorded as a function of wavelength at 45° angle of incidence and an out-of-plane magnetic field of 0.4 T in the 2 × 2 Jones matrix algorithm.
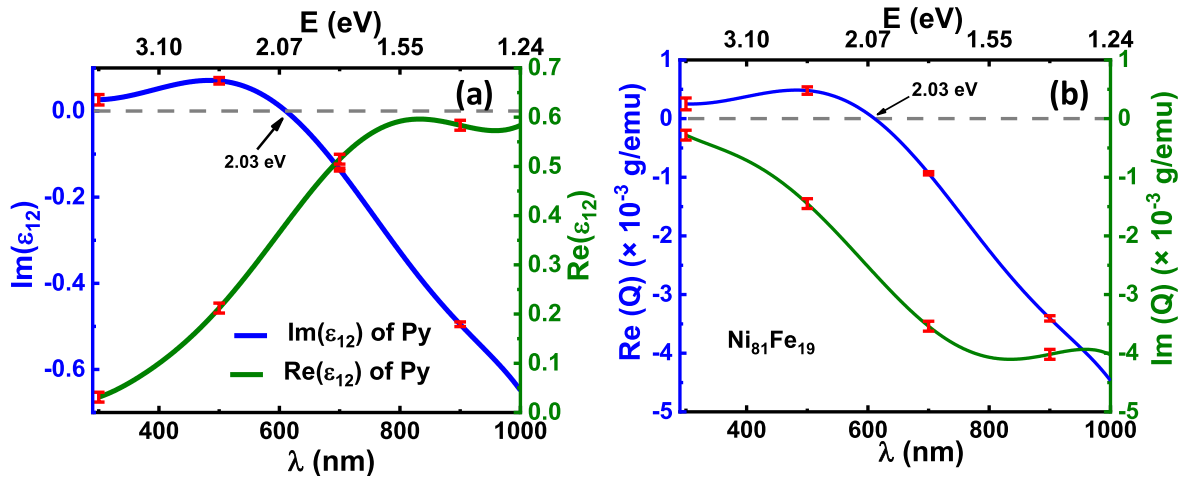

Figure 9. (a) Modelled complex off-diagonal elements of the dielectric tensor ε_{12} of Py which is same for the Py thin films in all six samples by fitting experimental differential Mueller matrix (ΔM_{14} and ΔM_{23}) spectra for all six samples (figure 7). Errors (red error bars) in the Mueller matrix difference data ($\delta(\Delta MM)$) are given at 300 nm, 500 nm, 700 nm and 900 nm. To be noted, Re(ε_{12}) is absorptive and Im(ε_{12}) is dispersive. The red error bars in the off-diagonal dielectric tensor ($\delta(\varepsilon_{12})$) are given at 300 nm, 500 nm, 700 nm and 900 nm. Note that the zero crossing position of the real part is found at 2.03 eV for both plots. (b) Calculated complex MO coupling constant, $Q(\lambda)$, of Py obtained by dividing the complex off-diagonal elements of the dielectric tensor ε_{12} of Py which is the same for all six samples by magnetization M (equation (9)), $M = 105 \pm 15$ emu g^{-1}. Calculated $Q(\lambda)$ of Py is the same for all six samples, i.e. independent of thickness and underlying substrate.

J. Phys. D: Appl. Phys. **52** (2019) 485002
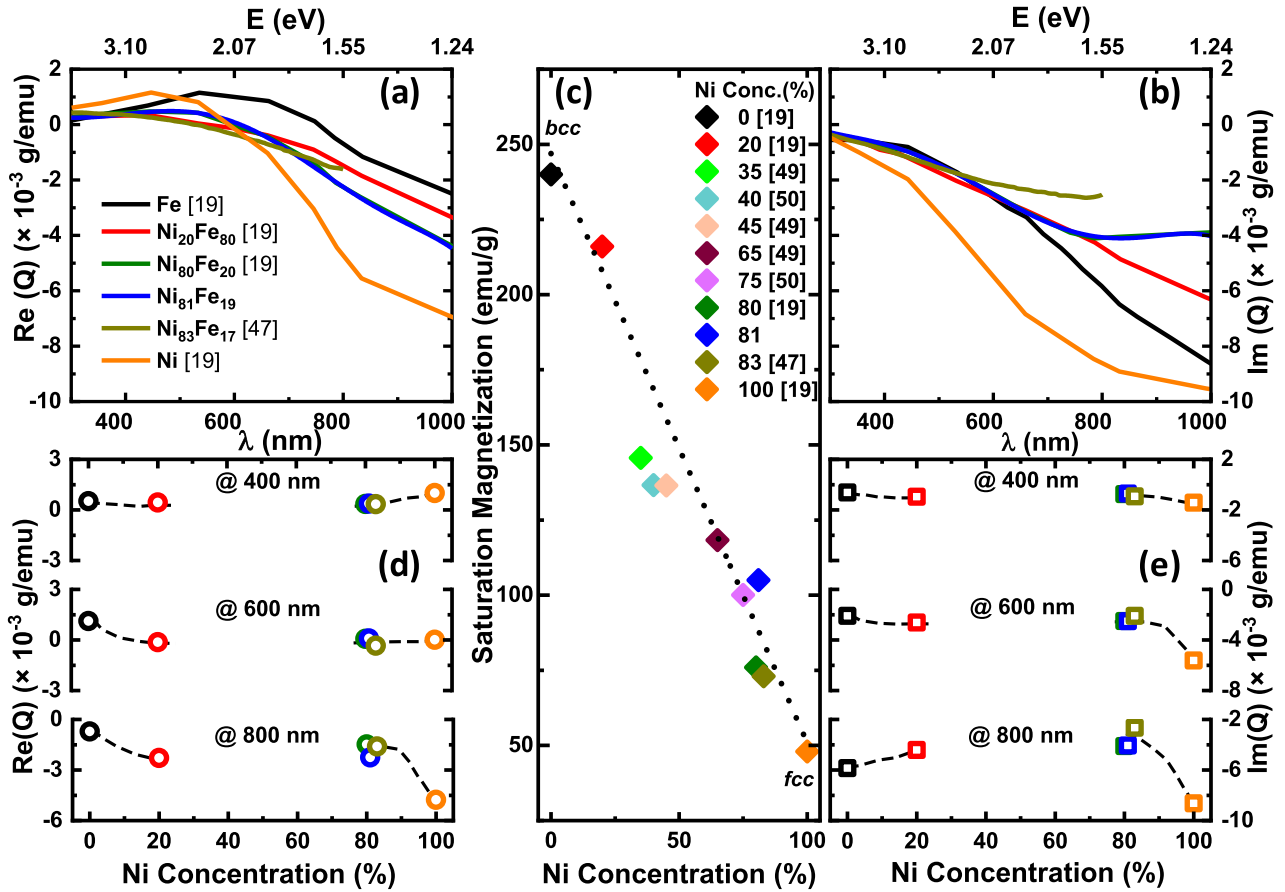
R Patra *et al*

Figure 10. Dependence of MO and magnetization property of Ni–Fe based alloys with Ni concentration in the range from 0 to 100%. Above 30% Ni concentration, the crystalline structure of Ni–Fe alloy changes from bcc to fcc [56, 57]. (a) Real and (b) imaginary part of complex MO coupling constant ($Q(\lambda)$) as obtained from the fitting (MSE = 0.817) of experimental differential Mueller matrix (ΔM_{14} and ΔM_{23}) spectra of Py_4 Si, Py_8 Si, and Py_{17} Si (figures 7(a)–(f)) and of Py_4 ZnO, Py_8 ZnO, and Py_{17} ZnO (figures 7(g)–(l)). MO coupling constant was ($Q(\lambda)$) found to be independent of thickness and underlying substrate. Literature values [19, 52] are also compared with the obtained results. Note that, Re($Q(\lambda)$) is absorptive and Im($Q(\lambda)$) is dispersive. (c) Saturation magnetization of Ni_xFe_{1-x} with variation of Ni concentration (%). This plot shows that the saturation magnetization can be linearly interpolated from the two saturation magnetization end points. (d) Real and (e) imaginary part of complex MO coupling constant at 400 nm, 600 nm and 800 nm versus Ni concentration (%). The MO coupling constant Q of Ni_xFe_{1-x} needs a nonlinear interpolation between the two Q end points. Therefore, even in a small alloy range the composition dependent Q of Ni_xFe_{1-x} can be only be interpolated if a sufficiently large number of Q values of analyzed Ni_xFe_{1-x} alloys is available. The dashed lines in (c)–(e) are for eye-guiding.

electron interband transitions between the *d*-bands of fcc Ni and of bcc Fe [59]. Furthermore, the contribution in the MO conductivity spectra has no visible influence as the transition between the majority states is very small. A broad feature in the imaginary part of the off-diagonal elements of the MO conductivity spectra is observed for both samples (green solid lines in figure 10) at 1.64 eV (754 nm), which is related to the disordered ferromagnetic Ni_3Fe peak. A similar peak has been observed by Nakajima *et al* at 1.5 eV for Ni [50] and by Singh at 1.7 eV for Fe [60]. Singh suggested that that this peak in Fe arises due to delocalized transitions from sufficiently large regions in the proximity of *N* points. Kulkova *et al* reported that the peak arises from a smoother shape of the minority-spin density of states (DOS) above the Fermi level in Ni_3Fe in comparison to fcc Ni (open circles in figure 11) and bcc Fe (open squares in figure 11) [59]. Disorder in Py causes a decrease in amplitude of both, real and imaginary parts of the off-diagonal elements of the MO conductivity tensor of Py with respect to that of individual element (fcc Ni and bcc Fe).

To summarize, there is agreement for the experimental and modelled angles $\Delta\theta_K$ and $\Delta\eta_K$, obtained from the 2 × 2 Jones matrix method in the spectral range between 300 nm and 1000 nm (figure 8) and between experimental and modelled ΔM_{14} and ΔM_{23} elements from the 4 × 4 Mueller matrix in the whole spectral range from 300 nm to 1000 nm (figure 7). A slight mismatch in the lower spectral range can be related with depolarization effects, which introduce an error if only the 2 × 2 Jones matrix, *J*, is analyzed. Using VMOGE measurements under magnetization values at 0.4 T, we have extracted the MO coupling constant $Q(\lambda)$ by modeling the dielectric tensor (equation (9)). Zero crossing positions were found at 2.03 eV form both, Q and from the off-diagonal conductivity spectra. The shift of the *d*-band to higher energies may causes shifting down of zero crossing energy at a lower value than pure Ni (5 eV) [40]. This red shift may further be attributed to a probable lattice mismatch at the Ru/Py and Py/Ta interfaces. The energy shifts in the *d*-band vigorously rely on lattice spacing and the atomic coordination number. The broad

J. Phys. D: Appl. Phys. **52** (2019) 485002
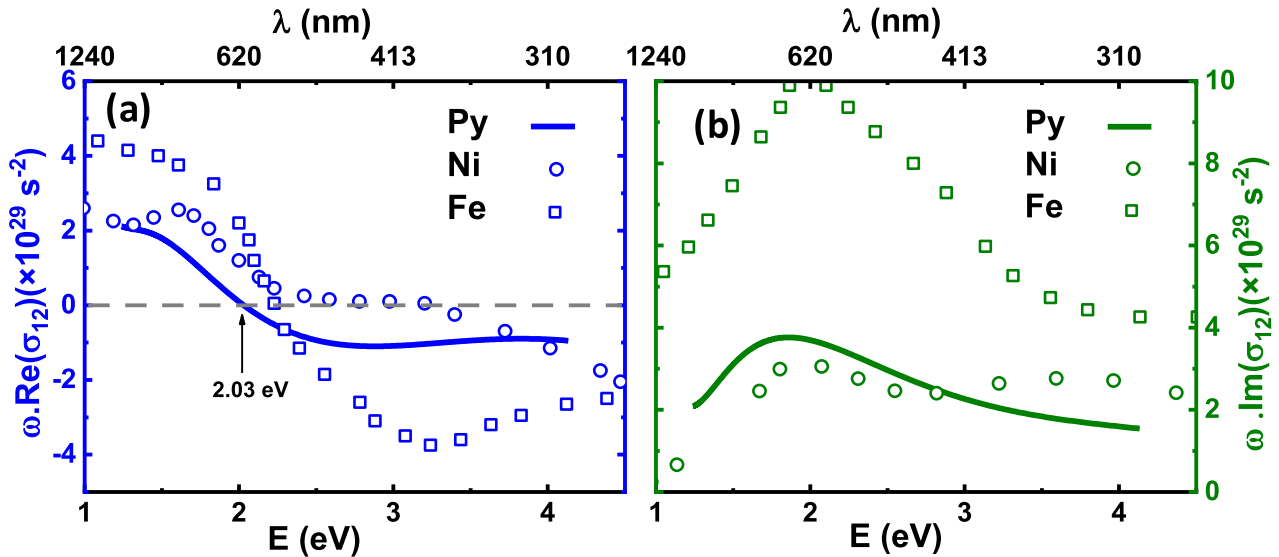
R Patra *et al*

Figure 11. Calculated (a) real and (b) imaginary part of complex off-diagonal elements of the MO conductivity matrix of Py of all six samples using the same complex off-diagonal elements of the dielectric tensor of Py of all six samples (figure 9(a)). Circles and squares in respective (blue and green) color show the corresponding (real and imaginary) conductivity data of fcc Ni and of bcc Fe, respectively [47]. Note that in contrast to figure 3, here, $Re(\sigma_{12})$ is dispersive and $Im(\sigma_{12})$ is absorptive.

peak at 754 nm (1.64 eV), found in the imaginary part of the MO conductivity spectra, is attributed to delocalized transitions from a sufficiently large region in the proximity of the N points and disordered ferromagnetic Ni_3Fe interband transitions and smoother minority-spin DOS above E_F as disorder in Ni_3Fe reduces the local magnetic moment. Figures 10(a) and (b) shows the extracted $Q(\lambda)$ dependency in agreement with the reported data. Furthermore, from figures 10(c)–(e) one can conclude that the saturation magnetization can be interpolated for any binary Ni–Fe alloy, though $Q(\lambda)$ can only be interpolated when the MO coupling constants for large enough Ni_xFe_{1-x} samples are accessible. Interpolated values of the magnetization saturation and $Q(\lambda)$ for a particular Ni_xFe_{1-x} alloy can be used to realize the wavelength dependence of the MO conductivity for that particular Ni–Fe alloy.

5. Conclusions and outlook

We have investigated the MO response of Py layers in same Ru/Py/Ta stacks on a SiO_2/Si substrate and on a ZnO substrate. XRD results reveal textured Py thin film growth on both substrates. The wavelength-dependent and material-specific MO coupling constant of a magnetizable thin film in a stack is independent of the thickness and of the underlying substrate. Furthermore, the interface roughness of the magnetic layer in the stack does not affect the extracted MO coupling constant. This finding allows for a different focus in the MO sensor development as compared to the focus in the TMR and GMR sensor development where interface roughness may be detrimental. Lattice mismatch at Ru/Py and Py/Ta interfaces may cause red-shift in the zero crossing position in Py compared to that of pure Ni. In summary, this study shows that the MO coupling constant of a magnetizable thin film in a stack is wavelength-dependent and material-specific. Therefore, the MO coupling constant is a bulk parameter

that cannot be linearly interpolated to binary Ni–Fe compounds. Finally, with the known MO coupling constant of a Ni_xFe_{1-x} thin films of a given chemical compositions the MO response of multilayer stacks containing corresponding Py layers can be predicted for different substrates and different Py thicknesses. The MO coupling constant does not depend on interface roughness. The complex MO coupling constant of Ni_xFe_{1-x} is found to be interoperable only for a large enough number of analyzed Ni_xFe_{1-x} alloys. The above results strongly suggest Ni_xFe_{1-x} thin films are potential candidates for MO sensors where the MO response is enhanced by controlling the MO contrast using Ni_xFe_{1-x} layers with different compositions.

ORCID iDs

Rajkumar Patra https://orcid.org/0000-0003-3406-6916
Georgeta Salvan https://orcid.org/0000-0002-2565-9675

References

[1] Binasch G, Grünberg P, Saurenbach F and Zinn W 1989 *Phys. Rev.* B **39** 4828

[2] Baibich M N, Broto J M, Fert A, Nguyen Van Dau F, Petroff F, Etienne P, Creuzet G, Friederich A and Chazelas J 1998 *Phys. Rev. Lett.* **61** 2472

[3] Kowalewski M *et al* 2000 *J. Appl. Phys.* **87** 5732

[4] Bader S D and Parkin S S P 2010 *Annu. Rev. Condens. Matter Phys.* **1** 71

[5] Kruglyak V, Demokritov S and Grundler D 2010 *J. Phys. D: Appl. Phys.* **43** 264001

[6] Choi B C, Xu H, Hajisalem G and Gordon R 2018 *Appl. Phys. Lett.* **112** 022403

[7] Ganguly A, Azzawi S, Saha S, King J A, Rowan-Robinson R M, Hindmarch A T, Sinha J, Atkinson D and Barman A 2015 *Sci. Rep.* **5** 17596

[8] Yu G H, Zhao H C, Li M H, Zhu F W and Lai W Y 2002 *Appl. Phys. Lett.* **80** 455

[9] Crawford T M, Rogers C T, Silva T J and Kim Y K 1996 *Appl. Phys. Lett.* **68** 1573

[10] Nembach H T, Livesey K L, Kostylev M P, Martin-Pimentel P, Hermsdoerfer S J, Leven B, Fassbender J and Hillebrands B 2011 *Phys. Rev.* B **84** 184413

[11] Choe G and Steinback M 1999 *J. Appl. Phys.* **85** 5777

[12] Saravanan P, Hsu J H, Tsai C L, Singh A K and Alagarsamy P 2015 *IEEE Trans. Magn.* **51** 2006604

[13] Ingvarssona S, Xiaoa G, Parkinb S S P and Gallagherc W J 2002 *J. Magn. Magn. Mater.* **251** 202

[14] Neshat M and Armitage N P 2013 *J. Infrared Milli Terahertz Waves* **34** 682

[15] Röseler A 1993 *Thin Solid Films* **234** 307

[16] Ferrieu F and Lecat J H 1990 *J. Electrochem. Soc.* **137** 2203

[17] Tompkins H G and Irene E A 2005 *Handbook of Ellipsometry* (Berlin: Springer)

[18] Fujiwara H 2007 *Spectroscopic Ellipsometry: Principles and Applications* (Chichester: Wiley)

[19] Heinze J, Frontana-Uribe B A and Ludwigs S 2010 *Chem. Rev.* **110** 4724

[20] Friedbacher G and Bubert H 2011 *Surface and Thin Film Analysis: a Compendium of Principles, Instrumentation, and Applications* (Weinheim: Wiley)

[21] Onsager L 1931 *Phys. Rev.* **37** 405

[22] Mok K, Kovacs G J, McCord J, Li L, Helm M and Schmidt H 2011 *Phys. Rev.* B **84** 094413

[23] Mok K, Scarlat C, Kovacs G J, Li L, Zviagin V, McCord J, Helm M and Schmidt H 2011 *J. Appl. Phys.* **110** 123110

[24] Postava K, Hrabovský D, Hamrlová J, Pištora J, Wawro A, Baczewski L T, Sveklo I and Maziewski A 2011 *Thin Solid Films* **519** 2627

[25] Rogers P D, Kang T D, Zhou T, Kotelyanskii M and Sirenko A A 2011 *Thin Solid Films* **519** 2668

[26] Herman L H, Kim C J, Wang Z, Jo M H and Park J 2012 *Appl. Phys. Lett.* **101** 123102

[27] Serber R 1933 *Phys. Rev.* **43** 1003

[28] Cloude S R 2013 *J. Opt. Soc. Am.* A **30** 691

[29] Buchmeier M, Schreiber R, Bürgler D E and Schneider C M 2009 *Phys. Rev.* B **79** 064402

[30] Mok K, Du N and Schmidt H 2011 *Rev. Sci. Instrum.* **82** 033112

[31] Tanaka S 1963 *Japan. J. Appl. Phys.* **2** 548

[32] Jung W 1965 *J. Appl. Phys.* **36** 2422

[33] Baek S, Dokukin M, Yayoi K, Baryshev A and Inoue M 2010 *J. Appl. Phys.* **107** 09A923

[34] Smith D O 1958 *J. Appl. Phys.* **29** 264

[35] Raposo V, Zazo M, Flores A G, Garcia J, Vega V, Iniguez J and Prida V M 2016 *J. Appl. Phys.* **119** 143903

[36] Langer J, Mattheis R, Ocker B, Maaß W, Senz S, Hesse D and Kräußlich J 2001 *J. Appl. Phys.* **90** 5126

[37] Fassbender J, von Borany J, Mücklich A, Potzger K, Möller W, McCord J, Schultz L and Mattheis R 2006 *Phys. Rev.* B **73** 184410

[38] Barholz K U and Mattheis R 2002 *J. Appl. Phys.* **91** 7224

[39] Srikant V and Clarke D R 1998 *J. Appl. Phys.* **83** 5447

[40] Tikuišis K K, Beran L, Cejpek P, Uhlířová K, Hamrle J, Vaňatka M, Urbánek M and Veis M 2017 *Mater. Des.* **114** 31

[41] Rakic A D, Djurisic A B, Elazar J M and Majewski M L 1998 *Appl. Opt.* **37** 5271

[42] Moravec T J, Rife J C and Dexter R N 1976 *Phys. Rev.* B **13** 3297

[43] Ehrenreich H, Philipp H R and Olechna D J 1963 *Phys. Rev.* **131** 2469

[44] Lynch D W, Rosei R and Weaver J H 1971 *Solid State Commun.* **9** 2195

[45] Smith N V, Lasser R and Chiang S 1982 *Phys. Rev.* B **25** 793

[46] Gao X, Woollam J A, Kirby R D, Sellmyer D J, Tanaka C T, Nowak J and Moodera J S 1991 *Phys. Rev.* B **59** 9965

[47] Delin A, Eriksson O, Johansson B, Auluck S and Wills J M 1999 *Phys. Rev.* B **60** 14105

[48] Zak J, Moog E R, Liu C and Bader S D 1991 *Phys. Rev.* B **43** 6423

[49] Ossikovski R 2011 *Opt. Lett.* **36** 2330

[50] Najikama K, Sawada H, Katayama T and Miyazaki T 1996 *Phys. Rev.* B **54** 15950

[51] Halilov S V and Uspenskii Y A 1990 *J. Phys.: Condens. Matter* **2** 6137

[52] Neuber G, Rauer R, Kunze J, Korn T, Pels C, Meier G, Merkt U, Bäckström J and Rübhausen M 2003 *Appl. Phys. Lett.* **83** 4509

[53] Woollam J A 2014 *CompleteEASE Software Manual* (Lincoln: J A Woollam)

[54] Chenna A, Benbrahim N, Hamadou L, Boudinar S, Kadri A, Chainet E and Dahmane Y 2018 *Surf. Eng.* **35** 189

[55] Dzhun I O, Babaytsev G V, Chechenin N G, Gritsenko C A and Rodionova V V 2019 *J. Magn. Magn. Mater.* **470** 151

[56] Chang W S, Wei Y, Guo J M and He F J 2012 *Open J. Metal* **2** 18

[57] Cacciamani G, Dinsdale A, Palumbo M and Pasturel A 2010 *Intermetallics* **18** 1148

[58] Huang J C A, Wang T E, Yu C C, Hu Y M, Lee P B and Yang M S 1997 *J. Cryst. Growth* **171** 442

[59] Kulkova S E, Valujskya D V, Kimb J S, Leeb G and Koo Y M 2002 *Physica* B **322** 236

[60] Singh M, Wang C S and Callaway J 1975 *Phys. Rev.* B **11** 287